Article

Enhancing Urban Flood Forecasting: Integrating Weather Forecasts and Hydrological Models

Yebing Liu [1,2], Luoyang Wang [1,2], Yihan Lou [1,2], Tangao Hu [1,2], Jiaxi Wu [1,2] and Huiyan Xu [1,2,*]

1   Institute of Remote Sensing and Earth Sciences, School of Information Science and Technology, Hangzhou Normal University, Hangzhou 311121, China; 2022111011004@stu.hznu.edu.cn (Y.L.); 2021111008046@stu.hznu.edu.cn (L.W.); 2022111011001@stu.hznu.edu.cn (Y.L.); hutangao@hznu.edu.cn (T.H.); 20231111011006@stu.hznu.edu.cn (J.W.)
2   Zhejiang Provincial Key Laboratory of Urban Wetlands and Regional Change, Hangzhou 311121, China
*   Correspondence: xuhuiyan613@hznu.edu.cn

Abstract: Precipitation data in urban hydrological models are derived from an ideal stormwater model, which has some uncertainties and limited prediction times. Therefore, to reliably forecast urban flooding, prolong prediction time periods, and better support associated research in urban flood forecasting, a combination of weather forecasts and urban hydrology is necessary. By applying comprehensive cloud microphysical schemes in the Weather Research and Forecasting (WRF) model to the predecessor torrential rainfall associated with Typhoon Khanun (2017), this study evaluated different configurations of atmospheric-hydrological simulations based on the WRF model and InfoWorks ICM. Results showed that the microphysics scheme could significantly affect spatial and temporal distributions of the simulated torrential rainfall. Generally, the combination of WRF and NSSL schemes produced better performance. Applying the NSSL scheme to the WRF model and combining it with the InfoWorks ICM system can reproduce torrential rainfall and urban flood formations.

Keywords: typhoon; torrential rainfall; urban floods

1. Introduction

With the intensification of global climate change, the frequency and intensity of typhoon rainfall have increased [1], resulting in substantial harm to human lives, property, and socioeconomic well-being. China is frequently affected by typhoons, with approximately seven to nine tropical cyclones making landfall annually in the densely populated and economically developed southeastern coastal areas [2]. Heavy precipitation caused either directly or indirectly by typhoons is of great concern to the public [3]. Numerous scientific research studies have been conducted over the years to investigate the physical processes affecting typhoon storms [1,3]. Typhoon rainstorms can be categorized into different rainfall patterns, such as heavy rainfall near the typhoon center, heavy rainfall outside the typhoon center, heavy rainfall in the typhoon spiral rainband, and typhoon-linked predecessor rainfall events (PREs). PREs are caused by the interaction between mid-latitude weather systems and typhoons over long distances [4] and occur almost every year in the Yangtze River Delta region of China [5]. In the Yangtze River Delta region, typhoon rainstorms frequently induce floods; thus, precise forecasting of events plays a crucial role in minimizing the economic losses and casualties caused by these events.

An accurate simulation of urban flooding relies primarily on the following three factors [6]: the impact of the spatial and temporal distributions of the simulated rainfall; errors in urban flooding models, such as InfoWorks ICM (Integrated Catchment Modeling), results from the physical processes of the model, and the calibration of sensitive parameters; and the complexity of the flood process, including factors such as flood peak size, presence or absence of base flow, and length of the recession process. Precipitation data for

research purposes are primarily sourced from historical or real-time observational data, data retrieved from weather radar or satellite remote sensing, and simulated data provided by the Weather Research and Forecasting (WRF) model [7]. Simulation studies on urban flooding often rely on rainfall data generated by statistical models or historical precipitation data; however, these types of data exhibit limitations in terms of research scale and data resolution [8]. The limited range and high cost of real-time observational data in urban flooding models hinder their utilization, presenting significant difficulties and challenges in improving the accuracy of flooding models [9]. On the other hand, the WRF model is a three-dimensional mesoscale numerical model that has been widely used in the simulation and analysis of precipitation [10] as it can reproduce heavy rainfall processes, generate precipitation with high spatial and temporal resolution [11], and further provide valuable support for regions lacking precipitation data.

Simulations using the WRF model are the principal method for investigating changes in weather and climate systems [11]. Cloud microphysical processes are the most important nonadiabatic heating physical processes [12], and their parameterization scheme can have a direct effect on convective system development and the accuracy of precipitation simulation [13]. Specifically, cloud microphysics schemes play a vital role in the dynamics of water vapor and condensed substances in the atmosphere, impacting processes like cloud formation, condensation, and precipitation. Effective cloud microphysics schemes enhance the prediction accuracy of atmospheric water vapor distribution and cloud characteristics, leading to improved accuracy in predicting precipitation events.

Many scholars have deployed the WRF model to conduct comparative experiments on precipitation processes using diverse cloud microphysical parameterization schemes and have explored their impact on precipitation simulations [14–16]. Various cloud microphysics schemes were found to possess distinct advantages in simulating precipitation of varying magnitudes, indicating that comprehending the effects of different cloud microphysics schemes on the simulation results of PREs is imperative. Simulated precipitation produced by diverse cloud microphysics schemes can serve as input data for urban heavy rain and flood models. Using precipitation data simulated by numerical models as inputs to hydrological models can extend the prediction period [17], providing data support for related research in areas with inadequate precipitation data. However, a certain degree of uncertainty exists in precipitation simulations using the meteorological models. The accuracy of the data from the models may significantly influence flooding simulations [18]. The impact of precipitation uncertainty, simulated by various cloud microphysical parameterization schemes, on flooding simulations, remains to be determined.

Currently, only a few studies have focused on the coupling of numerical atmospheric models with urban flood models [19,20], and even studies on the impact of precipitation simulated by different cloud microphysical parameterization schemes on the simulation of urban flooding are limited. Previous studies have shown that the selection of appropriate parameterizations may improve typhoon simulations in the Yangtze River Delta region [21–23]. The most recent research using this approach for hydrological forecasting has focused on coupling numerical atmospheric models with hydrological models such as the Xinanjiang model [24] and WRF-hydro model [25]. Gu et al. (2022) [26] conducted exciting experiments using WRF and SWMM models and yielded positive results that confirmed the feasibility of employing the method of coupling hydrological and meteorological models.

Typhoon Khanun (2017) made landfall in Guangdong Province, China, causing a torrential PRE in the Yangtze River Delta region. This study considered this case to compare and investigate the impact of different microphysical schemes on the precipitation intensity and spatial distribution of Typhoon Khanun and on the urban flooding simulations in the Yangtze River Delta region. By exploring the impact of the cloud microphysics scheme on the simulation of this particular precipitation event, this study revealed the underlying connection between typhoon precipitation and flooding caused by cloud microphysical processes, providing a reference for the accurate prediction of flooding caused by heavy rain.

2. Case Study and Data Description

2.1. Overview of the Typhoon Khanun Process

Typhoon Khanun (2017) caused a tropical disturbance in the western Pacific at 1200 UTC on 11 October 2017 [27], resulting in a landfall along the coast of the Philippines on eastern Luzon Island, Philippines, at 1900 UTC on 12 October. At the time of landfall, the maximum wind speed near the center reached up to 18 m·s^{-1}, and the minimum sea level pressure near the center was 995 hPa [28]. The disturbance moved westward, gradually forming and intensifying into a severe tropical storm at 1900 UTC on 13 October. It continued to move northwest, intensifying into a typhoon at 1400 UTC on the 14th and upgrading to a Category 2 typhoon at 0400 UTC on the 15th, with the maximum wind speed reaching 45.83 m·s^{-1} (Liu et al., 2022) [27]. It made a landfall on the coast of Xuwen County, Zhanjiang City, Guangdong Province, at around 1925 UTC on the 15th. At the time of landfall, the maximum wind speed near the center was up to 28 m·s^{-1}, and the minimum sea level pressure near the center was 988 hPa [29]. After moving into the Beibu Gulf, the typhoon's intensity gradually weakened and disappeared, and it stopped at 0900 UTC on 16 October. According to preliminary statistics from local governments, Typhoon Khanun caused direct economic losses of 23 million and 825 million yuan in Zhanjiang and Maoming, respectively.

Beside causing heavy rain disasters in South China, the typhoon interacted with short-wave troughs, causing extremely heavy rainfall in the Yangtze River Delta region [29]. From 14 to 16 October 2017, as Typhoon Khanun moved northwest and made landfall in Guangdong Province, torrential rainfall occurred in the northeastern Zhejiang Province. The cumulative rainfall generally exceeded 50 mm, with over 150 mm in the northeastern coastal areas, and the maximum accumulated rainfall at the Tantoushan Station in Ningbo was 467 mm. The torrential PRE caused by Typhoon Khanun (2017) in Zhejiang was listed as one of the top ten weather and climate events in Zhejiang Province in 2017.

2.2. Circulation Situation Analysis

This study used ERA5 data to draw the sea level pressure and wind fields at 200, 500, and 850 hPa geopotential heights and analyze the weather circulations during the PRE of Typhoon Khanun that occurred in the Yangtze River Delta region. Figure 1a,d show the wind and temperature fields at a 200 hPa geopotential height at 0000 UTC on 14 October and 0600 UTC on 15 October 2017, respectively. The 200 hPa circulation was zonally distributed in the mid- to high-latitudes of the Northern Hemisphere, with a deep low-pressure trough over the Sea of Okhotsk. The center of the subtropical high-pressure zone was located at 18° N, 120° E, with its main body to the west and south, and it had the advantage of outflow conditions for high-level divergence. The axis of the high-altitude jet stream is located near 38° N. The center of Typhoon Khanun was located at 18° N, 114° E, corresponding to a divergent airflow at 200 hPa, which was conducive to the westward extension of the subtropical high. By 0600 UTC on 15 October, the high-altitude jet stream shrank and narrowed, with the axis located near 40° N. This high-level divergence combined with bottom-level cyclonic convergence was conducive to a rapid rise in airflow in the eyewall and spiral rainbands, providing suitable dynamic conditions for typhoon precipitation.

Figure 1b,e show the wind and temperature fields at 500 hPa geopotential height for 0000 UTC on 14 October and 0600 UTC on 15 October 2017, respectively. This shows that the East Asian Great Trough extended from 39° N, 130° E, to 30° N, 120° E. The powerful western Pacific subtropical high was distributed in blocks, with the 592 dagpm line extending towards 124° E, and the typhoon's closed circulation could still be seen at 500 hPa (Figure 1b). By 0600 UTC on 15 October, as the low pressure in the mid- and high-latitudes moved eastward, the trough moved eastward and lifted northward, and the baroclinicity increased. As the high-level South Asian high moved eastward, the subtropical high extended westward and strengthened, with the ridge reaching 120° E. Typhoon Khanun was located on the southwest side of the 592 dagpm line of the subtropical high. Affected by the obstruction of the subtropical high and circulation configuration at mid- and high-latitudes, the typhoon moved northwest toward the coastal areas of South China.
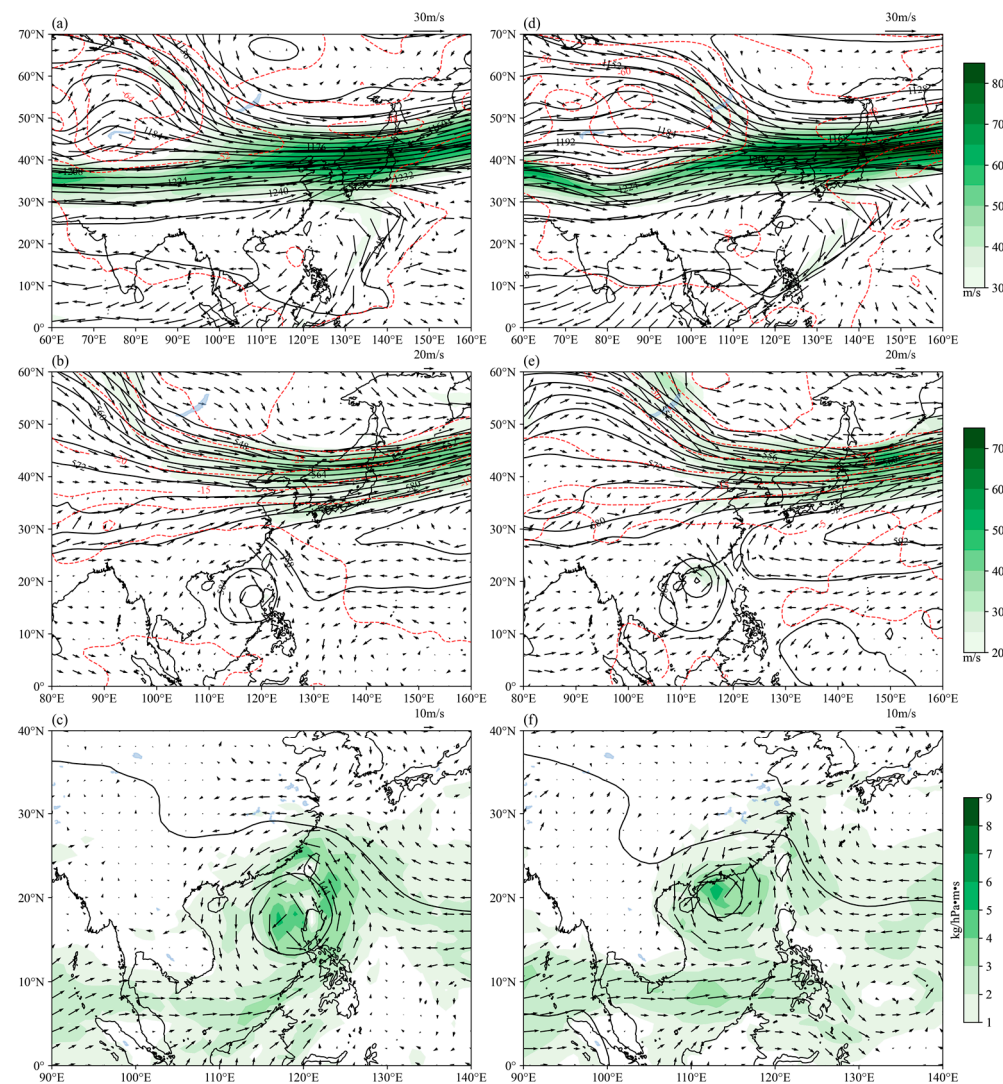
Figure 1. Synoptic circulations at different times: geopotential height (black contour lines; dagpm), temperature (red contour lines; °C), wind (vector; m·s^{-1}), and jet (colored; m·s^{-1}) at 200 hPa at (**a**) 0000 UTC on 14 October 2017 and (**d**) 0600 UTC on 15 October 2017; geopotential height field (black contour lines; dagpm), temperature field (red contour lines; °C), wind (vector; m·s^{-1}), and wind speed (colored; m·s^{-1}) at 500 hPa at (**b**) 0000 on 14 October 2017 and (**e**) 0600 UTC on 15 October 2017; geopotential height (black contour lines; dagpm), temperature field (red contour lines; °C), wind (vector; m/s), and water vapor flux (colored; kg·hPa^{-1}·m^{-1}·s^{-1}) at (**c**) 850 hPa at 0000 UTC on 14 October 2017 and (**f**) 0600 UTC on 15 October 2017.

Figure 1c,f show the wind field and water vapor flux at an 850 hPa geopotential height for 0000 UTC on 14 October and 0600 UTC on 15 October 2017. On 14 October, the sources of typhoon water vapor were mainly southwestern and southeastern warm and humid air brought by the cross-equatorial airflow of the southwest monsoon and the southwest side of the subtropical high, respectively. The abundant water vapor transport at this time was conducive to the further development and strengthening of typhoons (Figure 1c). By 15 October, as the typhoon moved and its latitude increased, water vapor transported by the cross-equatorial airflow became unimportant. Strong southwesterly moisture from the Bay of Bengal via the Indochina Peninsula began to affect Khanun, and simultaneously, the southeasterly moisture on the southwest side of the subtropical high was connected to the typhoon. Southwesterly and southeasterly water vapors continuously transported to the typhoon, providing abundant energy and water vapor sources for the typhoon, which was favorable for the offshore strengthening of Khanun [28,29].

3. Methods

3.1. Weather Research and Forecasting Model

Taking the EAR5 reanalysis data (1° × 1°) as the background initial field, the WRF numerical model was used to simulate Typhoon Khanun (2017). The simulation time was from 0000 UTC on 14 October to 0000 UTC on 16 October 2017. This period included the development, intensification, and northwestern movement of the typhoon after making landfall in Guangdong. The detailed model configuration scheme is presented in Table 1. Five simulation domains were used, and the detailed nesting areas are shown in Figure 2. The flowchart was showed in Figure 3.

Table 1. Summary of different numerical experiments.

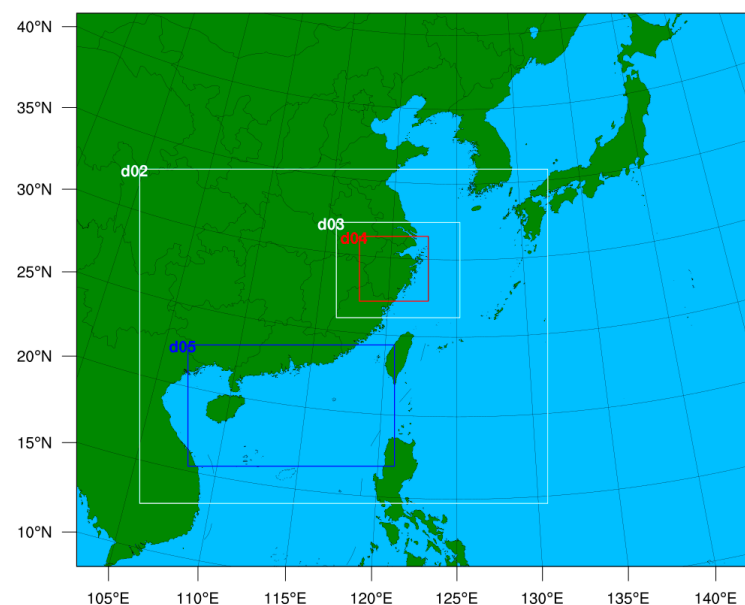| Configuration	Options
Initial Filed	ERA5 reanalysis data (1° × 1°)
Nesting Options	D01: 184 × 150 × 35; D02:331 × 271 × 35; D03:301 × 232 × 35; D04: 502 × 472 × 35; D05: 502 × 295 × 35
Center Point	(25° N, 121° E)
Resolutions	27 km (d01); 9 km (d02); 3 km (d03); 1 km (d04); 3 km (d05)
The top of the vertical height	20 hPa
Vertical layers	35
Microphysical schemes	WSM6; Purdue-Lin; Milbrandt-Yau; WDM6; Thompson; NSSL; Morrison; SBU_YLin; P3
Cumulus Parameterization	Grell–Devenyi
Radiation schemes	RRTMG
Land-Surface Models	Noah
Planetary Boundary Layer schemes	YSU

Figure 2. Map of model domains.

The Purdue–Lin scheme (Lin) is derived from the Purdue cloud model and six species of hydrometeor (water vapor, cloud water, rain, cloud ice, snow, and graupel) are included, which are more suitable for research purposes [30]. The WRF single-moment 6-class graupel scheme (WSM6) is an extension of the WSM5 scheme, which adds graupel and its related processes [31]. It is a scheme suitable for high-resolution processes involving ice and snow. The Milbrandt–Yau 2-moment scheme (Milbrandt–Yau) is a fully double-moment

scheme that carries graupel and hail as separate species, enabling the depiction of complex convective weather processes at both mid and small scales [32,33]. The SBU_YLin 5-class scheme (SBU_YLin) is an adaptation of the Lin scheme. It predicts two types of ice-phase particles and replaces snow and graupel with ice crystals and sedimenting ice, which significantly improves computational efficiency [34]. The WRF double-moment 6-class scheme (WDM6) is a double-moment scheme. It adds forecasts for cloud-condensation nuclei (CCNs) concentrations to analyze aerosol impacts on cloud properties and precipitation processes [35]. The NSSL 2-moment scheme with CCN Prediction (NSSL) is a double-moment scheme forecasting average graupel concentration, which ensures a good distribution of graupel particles even in freezing rain conditions [36]. The Aerosol-aware Thompson scheme (Thompson) is a bulk microphysics scheme that includes ice and rain, predicting their number concentrations [37]. The Morrison double-moment scheme (Morrison) is a mixed-phase double-moment scheme, accurately forecasting convective weather and aerosols at small to mid scales. It is suitable for studying aerosol effects on convective weather [38]. The Predicted Particle Properties scheme (P3) predicts the transition of ice particles into snow or graupel, which can optionally choose a double-moment cloud to handle aerosol effects [39]. The Spectral Bin Microphysics scheme (SBM) categorizes cloud droplets, precipitation particles, and other microscopic particles into various spectral bins to enhance the precision of describing and simulating the formation and progression of clouds and precipitation [40]. All the models, microphysical schemes, and datasets utilized in the study are summarized in Table 2.
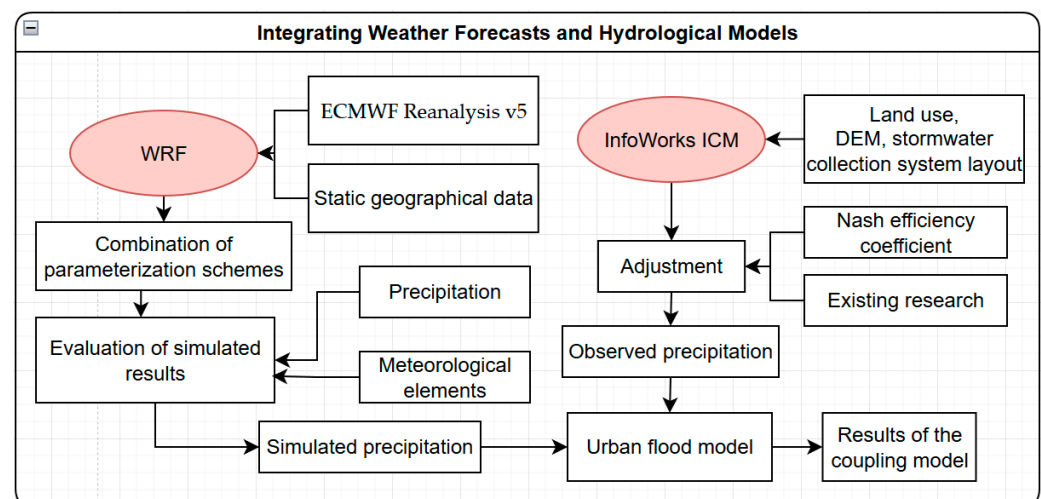

Figure 3. Framework of integrating weather forecasts and hydrological models.

Table 2. Summary of abbreviations applied in the study.

Item	Full Name	Reference
Lin	The Purdue–Lin scheme	[30]
WSM6	The WRF single-moment 6-class graupel scheme	[31]
Milbrandt–Yau	The Milbrandt–Yau 2-moment scheme	[32,33]
SBU_YLin	The SBU_YLin 5-class scheme	[34]
WDM6	The WRF double-moment 6-class scheme	[35]
NSSL	The NSSL 2-moment scheme with CCNs Prediction	[36]
Thompson	The Aerosol-aware Thompson scheme	[37]
Morrison	The Morrison double-moment scheme	[38]
P3	The Predicted Particle Properties scheme	[39]
SBM	The Spectral Bin Microphysics scheme	[40]
PREs	Predecessor Rain Events	/
InfoWorks ICM	Integrated Catchment Modeling	/
WRF	Weather Research and Forecasting model	/
ERA5	ECMWF (European Centre for Medium-Range Weather Forecasts) Reanalysis V5	/

3.2. InfoWorks ICM Modeling

InfoWorks ICM 2023.0.0 is drainage model software developed by Innovyze that has been widely used for urban drainage system assessment and urban flood risk evaluation [41]. It can combine the urban drainage pipe network system model and river model and more realistically simulate the interaction between the underground drainage pipe network system and the surface water body. Prior to flood hazard mapping, real historical flood events were selected for model calibration and validation, which is crucial for reliable prediction modeling. The InfoWorks ICM simulates the diffusion and transport of stream flow in a one-dimensional pipeline by completely solving the de Saint-Venant system of equations. The mathematical expression of the de Saint-Venant equation is as follows:

$$\begin{cases} \frac{\partial A}{\partial t} + \frac{\partial Q}{\partial x} = 0, \\ \frac{\partial Q}{\partial t} + \frac{\partial}{\partial x}\left(\frac{Q^2}{A}\right) + gA\left(\cos\theta\frac{\partial h}{\partial x} - S_0 + \frac{Q|Q|}{K^2}\right) = 0 \end{cases} \tag{1}$$

where A represents the cross-sectional area of the pipe (m^2); Q represents the flow rate of the fluid (m^3/s); t represents the time (s); x represents the length of the pipe along the direction of water flow (m); g represents the acceleration due to gravity (in meters per square second); θ represents the angle between the center line of the pipeline and the horizontal line (°); h represents the water level (m); S_0 represents the slope of the bottom of the channel; and K represents the water transport rate determined by Manning's formula.

In the InfoWorks ICM, 540 junctions, 611 conduits, and 517 sub-catchments were built. The streamflow processes at a block in Haining City were selected as the inflow boundaries for the model. The values of the main parameters used in the InfoWorks ICM are listed in Table 3.

Table 3. Parameter attributes of five different types of runoff surfaces [42].

Number of Flow Generating Surface	Flow Generating Surface	Runoff Type	Fixed Runoff Coefficient	Initial Loss Type	Initial Loss Value	Runoff Coefficient
1	Roads	Fixed	0.9	Abs [1]	0.002	0.018
2	Buildings	Fixed	0.8	Abs	0.001	0.020
3	Greenery	Horton	/	Abs	0.0030	0.030
4	Bare ground	Horton	/	Abs	0.0025	0.040
5	Others	Fixed	0.5	Abs	0.0050	0.025

Note: [1] Abs: Absolute Infiltration Model.

The urban flooding simulations were conducted as follows: First, the generalized pipe network data were input into the InfoWorks ICM, and software tools were used to check the connectivity of the pipelines. Next, the divided sub-catchment area data were input into the model, and the related attributes of different runoff-generating surfaces were input based on land-use type. An automatic area extraction tool was used to calculate the proportions of different runoff-generating surfaces in each sub-catchment area. Finally, the precipitation data were input, and one-dimensional simulation calculations were performed.

3.3. Statistical Methods

The threat score (*TS*) method is a common meteorological evaluation metric employed to evaluate the accuracy of precipitation forecasts, focusing on the correct prediction of positive events (e.g., rainfall) from the total observed positive events, and is calculated using the number of hits, misses, and false alarms. Correspondingly, a higher *TS* score indicates better forecast accuracy.

The formula for the *TS* is as follows [43]:

$$TS = \frac{N_a}{N_a + N_b + N_c} \tag{2}$$

where N_a is the number of samples in which both simulated and observed rainfall appear within a certain precipitation level; N_b is the number of samples in which the simulations appear but observations do not; and N_c is the number of samples in which the simulations appear but observations do not.

In addition to the *TS* method, the statistical methods in Table 4 were applied. The Nash efficiency coefficient (*NSE*) was applied for the evaluation of hydrological model performance [26]. The relative error of peak streamflow (*REP*) and the absolute error of the time of peak occurrence (*AET*), in reference to Gu et al. (2022) [26], were applied. In reference to Tan et al. (2018) [44], the Pearson correlation coefficient (*PCC*), root mean square error (*RMSE*), and mean bias error (*MBE*) were used to evaluate the model performance on temporal scales.

Table 4. Statistical methods applied in the study.

Name (Symbol)	Formula	Optimal Value
The Nash efficiency coefficient (NSE)	$NSE = 1 - \dfrac{\sum\limits_{i=1}^{N}\left(Q_i^{sim} - \overline{Q^{obs}}\right)^2}{\sum\limits_{i=1}^{N}\left(Q_i^{obs} - \overline{Q^{obs}}\right)^2}$	1
The relative error of peak streamflow (REP)	$REp = \dfrac{\left|Q_p^{obs} - Q_p^{sim}\right|}{Q_p^{obs}} \times 100\%$	0
The absolute error of the time of peak occurrence (AET)	$AEt = T_p^{obs} - T_p^{sim}$	0
Pearson correlation coefficient (PCC)	$PCC = \dfrac{\sum\left(Q_i^{obs} - \overline{Q^{obs}}\right)\sum\left(Q_i^{sim} - \overline{Q^{sim}}\right)}{\sqrt{\sum\left(Q_i^{obs} - \overline{Q^{obs}}\right)^2 \sum\left(Q_i^{sim} - \overline{Q^{sim}}\right)^2}}$	1
Root mean square error (RMSE)	$RMSE = \sqrt{\dfrac{1}{N}\sum\limits_{i=1}^{N}\left(Q_i^{obs} - Q_i^{sim}\right)^2}$	0
Mean bias error (MBE)	$MBE = \dfrac{1}{N}\sum\limits_{i=1}^{N}\left(Q_i^{obs} - Q_i^{sim}\right)$	0

Notes: Q_i^{obs} and Q_i^{sim} are the *i*-th observed and simulated variable; N is the number of observations; and $\overline{Q^{obs}}$ is the averaged value of observations. Q_p^{obs} is the observed peak streamflow ($m^3 \cdot s^{-1}$) and Q_p^{sim} is the simulated peak streamflow ($m^3 \cdot s^{-1}$). T_p^{obs} is the observed time of peak occurrence and T_p^{sim} is the simulated time of peak occurrence.

4. Results and Discussion

4.1. Comparative Analysis of Meteorological Elements

4.1.1. Simulation Test of Horizontal Basic Elements

Figure 4a,c show the heat maps of the correlation coefficient and RMSE between the observed and simulated geopotential heights from different cloud microphysics schemes at different periods in the outermost domain. The correlation coefficients and errors of the observed and simulated geopotential heights at the initial moment from the different schemes were consistent. After 12 h of model integration, the correlation between the simulation and observations increased and the RMSE decreased. The correlation coefficient between the observed and simulated geopotential heights from all cloud microphysics schemes exceeded 98%, and the RMSEs did not exceed 2.4 dagpm. Although the correlation coefficient of all schemes was approximately 0.97 after 36 h of model integration, the RMSEs were within 2.4 dagpm, and the geopotential heights simulated by different cloud microphysics schemes only showed slight differences (Table 2). This indicates that all cloud microphysics schemes can reproduce the 500 hPa geopotential height fields well.

Figure 4b,d show the heat maps of the correlation coefficient and RMSE between the observed and simulated wind speeds from different cloud microphysics schemes at different periods in the outermost domain. The correlation coefficient between the wind speed and the observations at the start of the simulation was higher than 0.98, and the RMSE was 1.83 m·s^{-1}, indicating that the wind field at the initial time was close to the observations. On comparing the geopotential heights, as the integration time increased, the correlation coefficient between the simulated and observed wind speeds decreased, and the values were approximately distributed between 0.92 and 0.97. The RMSEs between the simulated and observed values increased, and the values were roughly distributed between 2.64 and 3.65 m·s^{-1}. Generally, the 500 hPa wind field simulated by different cloud microphysics schemes was similar to what was observed. Simultaneously, the difference between each scheme did not exceed 0.2 m·s^{-1} (Table 5), indicating that all other cloud microphysics schemes can also appropriately reproduce the 500 hPa wind speed.
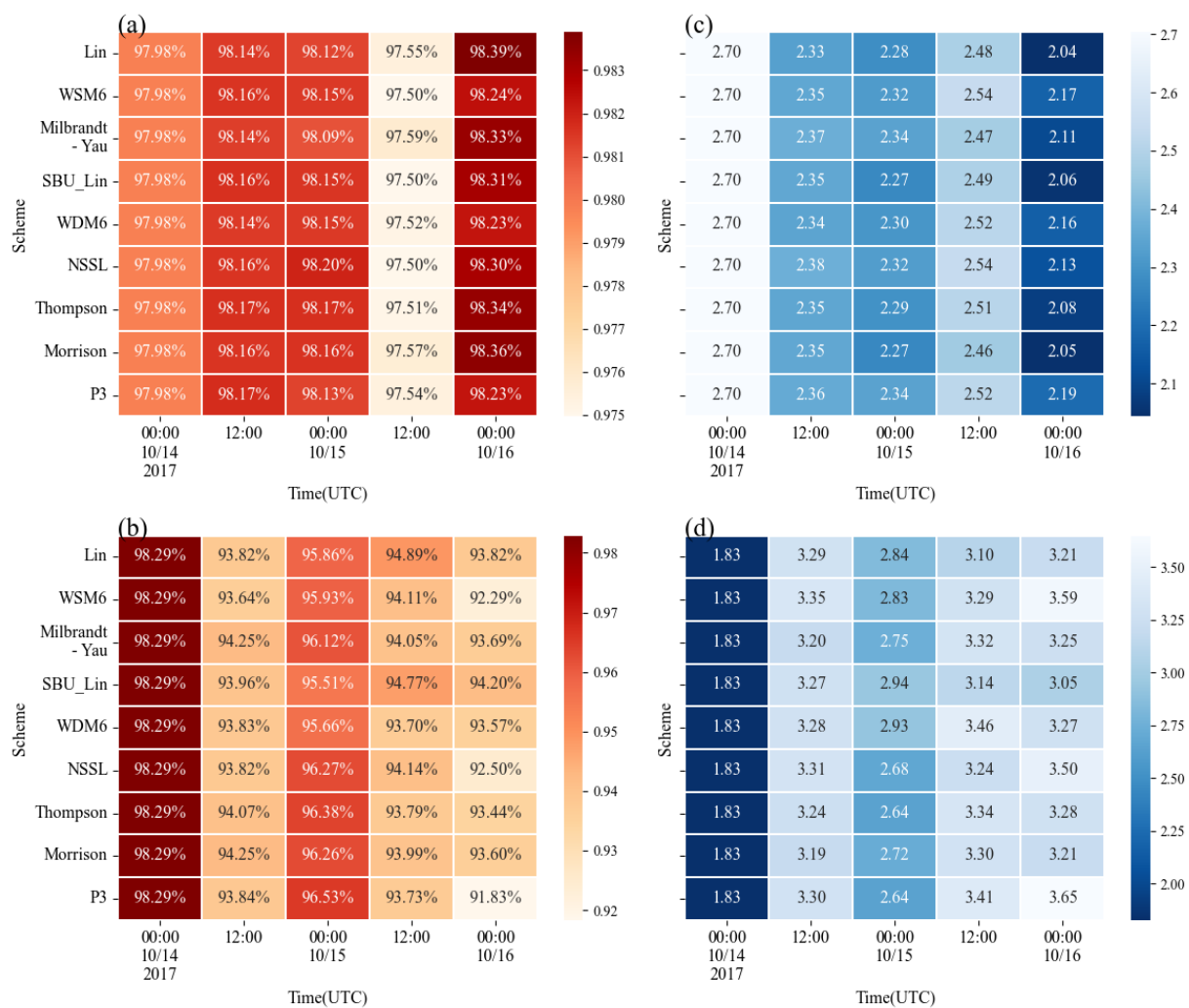

Figure 4. Statistical results of meteorological elements in the d01 area simulated by different cloud microphysics schemes at different time periods: (**a**) correlation coefficient between simulated 500 hPa geopotential height and observations; (**b**) root mean square error between simulated 500 hPa geopotential height and observations (dagpm); (**c**) correlation coefficient between simulated 500 hPa wind speed and observations; (**d**) root mean square error between simulated 500 hPa wind speed and observations (m·s^{-1}).

Table 5. Averaged correlation and root mean square error of meteorological fields between the observations and simulations from different cloud microphysics schemes.

Variables	Methods	Lin	WSM6	Milbrandt–Yau	SBU_Y Lin	WDM6	NSSL	Thompson	Morrison	P3
Geo-potential height field	PCC	0.98	0.98	0.98	0.98	0.98	0.98	0.98	0.98	0.98
	RMSE	2.37	2.42	2.40	2.37	2.41	2.41	2.39	2.37	2.42
Wind field	PCC	0.95	0.95	0.95	0.95	0.95	0.95	0.95	0.95	0.95
	RMSE	2.85	2.98	2.87	2.85	2.95	2.91	2.87	2.85	2.97
Temperature	PCC	1.00	1.00	1.00	1.00	1.00	1.00	1.00	1.00	1.00
	RMSE	0.82	0.82	0.80	0.75	0.89	0.80	0.83	0.77	0.84
Water vapor mixing ratio	PCC	1.00	1.00	1.00	1.00	1.00	1.00	1.00	1.00	1.00
	RMSE	0.65	0.62	0.68	0.61	0.64	0.67	0.66	0.63	0.64

4.1.2. Simulation Test of Vertical Basic Elements

Figure 5a,c show the heat maps of the correlation coefficient and RMSE between the observations and the temperature fields. This study interpolated the simulations of different cloud microphysics schemes in different periods to the four observation stations of Hangzhou, Baoshan, Hongjia, and Quzhou, and simulated averaged values were compared with the observations. All scheme simulations captured the observed temperatures during different periods. The correlation coefficient between simulation and observations was close to 0.99, and the RMSE value was less than 0.5 °C. Especially at 0000 UTC on 16 October, the WDM6 scheme simulated the temperature closest to the observations, with an RMSE of 0.21 °C, followed by WSM6, NSSL, Lin, and Milbrandt–Yau schemes, which also well reproduced the observed temperature.
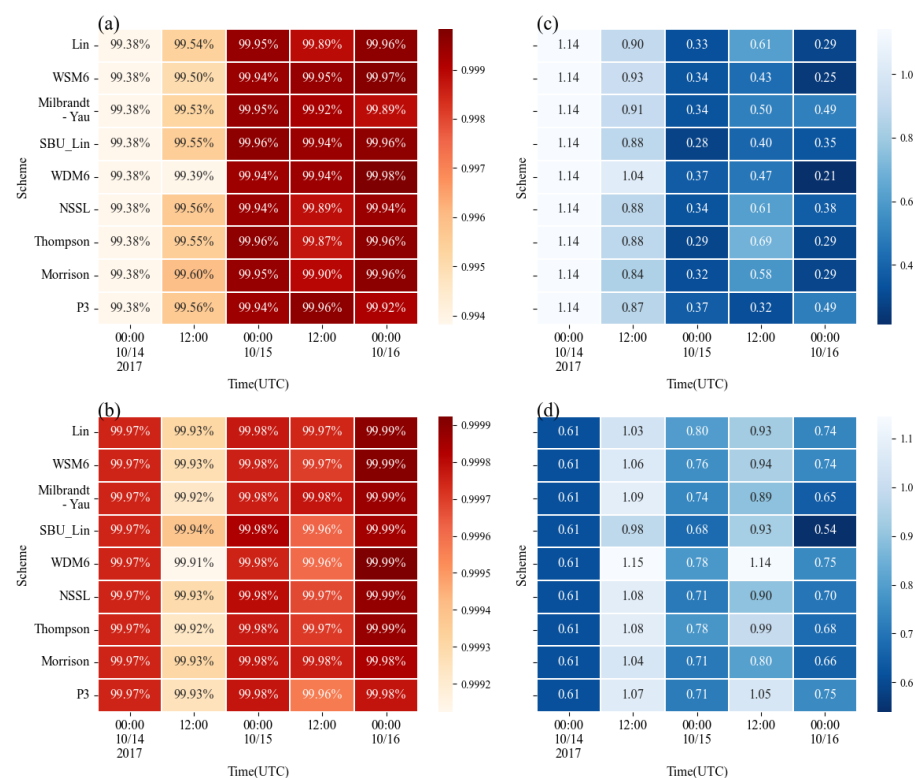

Figure 5. Statistical results of meteorological elements between observations and simulations simulated by different cloud microphysics schemes at different time periods at four basic meteorological stations in Hangzhou, Baoshan, Hongjia, and Quzhou: (**a**) correlation coefficient between the simulated temperature and observations; (**b**) root mean square error between the simulated temperature and the observation (unit: °C); (**c**) correlation coefficient between the simulated water vapor mixing ratio and observations; (**d**) root mean square error between the simulated water vapor mixing ratio and observations (g·kg^{-1}).

Figure 5b,d show heat maps of the correlation coefficient and RMSE between the simulated water vapor mixing ratio and the observations. The simulation results of different cloud microphysics schemes were interpolated to the four observation stations of Hangzhou, Baoshan, Hongjia, and Quzhou, averaged for different periods, and compared with the observations. The related coefficients of the water vapor mixing ratio of all schemes decreased slightly after 12 h integrations, and the simulations of different cloud microphysical schemes for the temperature and water vapor mixing ratio at different stations were generally preferable. The correlation coefficient was greater than 0.99 and the RMSE was 0.54–0.75 $g \cdot kg^{-1}$. Overall, the performance of the NSSL scheme was relatively stable.

4.2. Analysis of Precipitation Simulation Results

4.2.1. Comparison of Precipitation Simulation Results

Figure 6 shows the 36 h cumulative rainfall and simulation results from 0000 UTC on 14 October to 0000 UTC on 16 October 2017. A comparative analysis of the simulated and actual precipitation was conducted as follows. Figure 6k shows that after Typhoon Khanun made landfall, heavy precipitation was mainly concentrated in the Yangtze River Delta region (heavy rain area A) and eastern Zhejiang Sea (heavy rain area B). The maximum rainfall at 36 h exceeded 400 mm, and the distribution of heavy precipitation areas was generally consistent with the coastline. In general, the WDM6 scheme underestimated heavy rainfall in Zhoushan, whereas the other eight cloud microphysics schemes generally reproduced both heavy rain areas A and B, whereas the spatial distribution showed certain differences. Specifically, the coverage area of heavy rain Zone B was overestimated by all nine cloud microphysics schemes. In particular, the area coverage of heavy rain Zone B by Milbrandt–Yau, WDM6, and SBM was significantly overestimated. In contrast, the values simulated by Purdue–Lin, WSM6, SBU-YLin, and NSSL schemes were closer to the observations. Generally, in terms of intensity and rainfall area, the NSSL scheme was the closest to the observations, followed by the Purdue–Lin scheme and WSM6 scheme.

4.2.2. Precipitation Simulation Test

To quantitatively analyze the precipitation simulations from nine different cloud microphysics schemes and further examine the impact of cloud microphysics schemes on precipitation simulations, the simulated 36 h precipitation was interpolated to the observation stations and evaluated using the TS method. Considering that the maximum 36 h accumulated rainfall of the typhoon exceeded 400 mm, the precipitation was divided into six levels, as shown in Table 6.

Table 6. Different precipitation levels.

Rainfall Level	24 h Cumulative Rainfall (mm)
Light rain	≥0.1
Moderate rain	≥10
Heavy rain	≥25
Torrential rain	≥50
Heavy torrential rain	≥100
Extreme torrential rain	≥250

The TS scores of the nine microphysics schemes showed that different cloud microphysics schemes generally reproduced light rain well, and the TS values gradually decreased from light rain to extreme precipitation levels (Table 7). Previous research shows that extreme precipitation associated with PREs generally occurs in a local area and covers a small spatial range [45] (Yuan et al., 2018). Meanwhile, the accurate prediction of local heavy rainfall is not only related to cloud microphysics, but also relies on the resolution of models [46] (H. Xu, Li, Yin, Zhou, et al., 2023), and the moisture transport at the lower-to-mid levels will also affect the simulation results of extreme precipitation events [47] (Liu et al., 2023). As rainfall increased, the disparity in TS values among

various schemes progressively increased, indicating that the precipitation magnitude increased the sensitivity of the model to cloud microphysical processes. Overall, neither the single-moment nor double-moment microphysical scheme was ideal for simulating heavy precipitation, and the TS results of extremely heavy rainstorms were all lower than 0.12. After excluding the first 12 h of the model start-up time, the simulation improved to varying degrees, except for the Lin scheme. For moderate rainfall, the SBU_YLin scheme yielded preferable simulation results. For heavy rain and above, the NSSL scheme was generally better than the other schemes, indicating that the NSSL scheme has certain advantages for heavy rainfall simulations. Although WDM6 exhibits certain advantages in simulating heavy rainfall, it failed to capture heavy rainfall in the Yangtze River Delta region. Considering the averaged TS values and spatial distributions of rainfall, the NSSL, WSM6, and Lin schemes generally reproduced the PRE rainfall well.
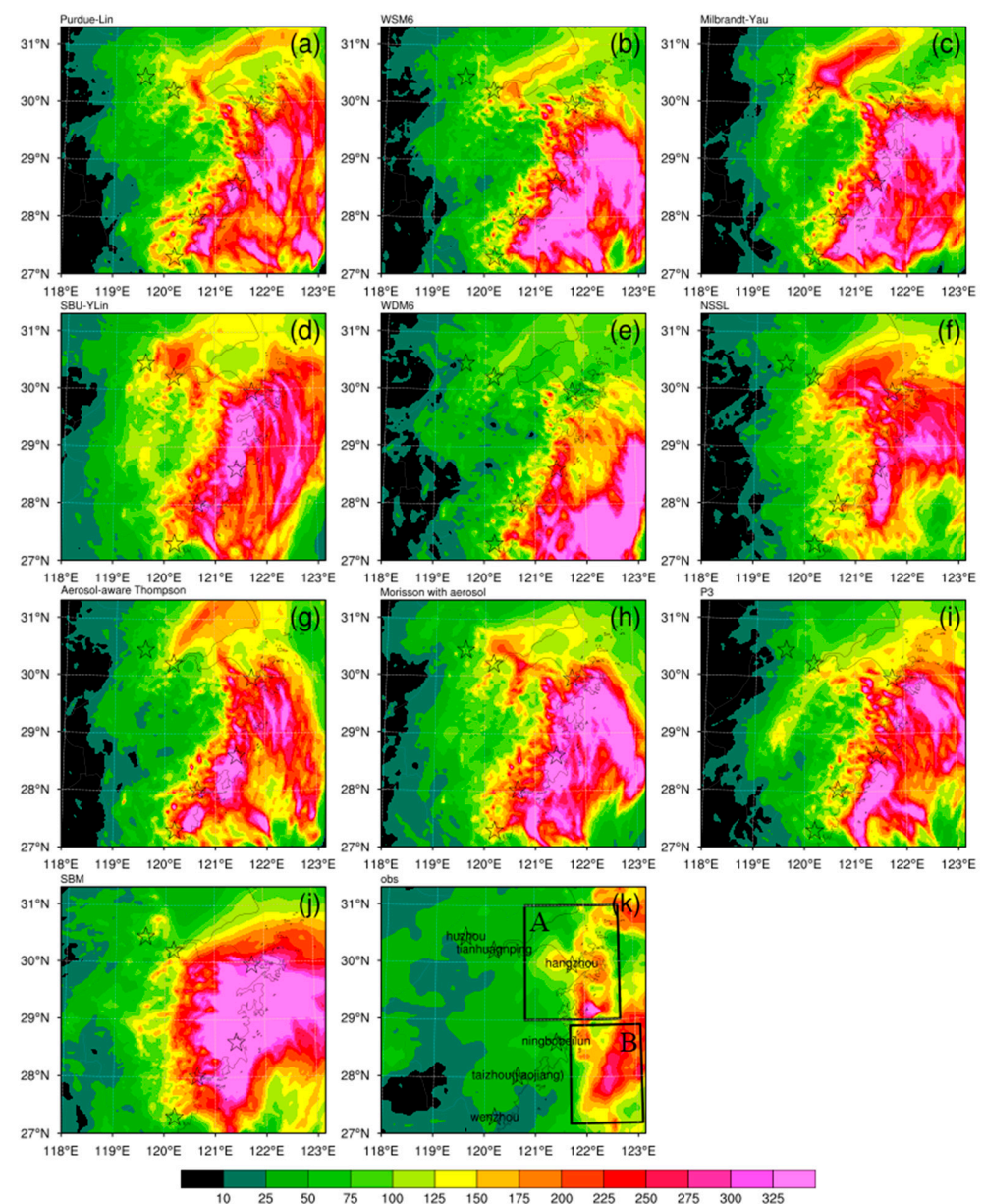

Figure 6. Simulated cumulative rainfall from 1200 UTC on 14 October to 0000 UTC on 16 October 2017 with (**a**) Purdue-Lin, (**b**) WSM6, (**c**) Milbrandt-Yau, (**d**) SBU-YLin, (**e**) WDM6, (**f**) NSSL, (**g**) Aerosol-awared Thompson, (**h**) Morisson with aerosol, (**i**) P3, (**j**) SBM schemes, and that of (**k**) observations. The stars represent the locations of the cities. The rectangle represents the heavy rainfall domains mentioned in the context.

Table 7. Threat score (TS) of different levels of precipitation for different microphysical schemes from 1200 UTC, 14 October to 0000 UTC, 16 October 2017.

Precipitation	Lin	WSM6	Milbrandt–Yau	SBU_YLin	WDM6	NSSL	Thompson	Morrison	P3	Averaged
Light rain	0.99	0.99	0.99	0.99	0.96	0.99	0.99	0.99	0.99	0.99
Moderate rain	0.77	0.78	**0.81**	0.85	0.74	0.76	0.78	0.80	0.75	0.78
Heavy rain	0.74	0.73	0.66	0.71	0.72	**0.75**	0.76	0.72	0.70	0.72
Torrential rain	0.56	0.56	0.46	0.54	0.60	0.60	0.52	0.51	**0.58**	0.55
Heavy torrential rain	0.43	0.49	0.38	0.42	0.54	**0.53**	0.35	0.39	0.41	0.44
Extreme torrential rain	**0.11**	**0.11**	0.09	**0.11**	**0.11**	0.12	0.10	0.09	0.12	0.11
Averaged	0.60	**0.61**	0.57	0.60	**0.61**	0.63	0.58	0.58	0.59	0.60

Note: Red denotes the best, bold denotes the secondary best.

4.3. Analysis of Streamflow Simulation Results

The precipitation histogram in Figure 7a shows the 6 h cumulative precipitation every 6 h. This shows that peak precipitation occurred on 15 October, which is consistent with the real peak precipitation time. The SBU_YLin, WSM6, and Thompson schemes simulated higher precipitation than those of other schemes, whereas NSSL, Lin, Morrison, and Milbrandt–Yau schemes overestimated precipitation at 06:00 UTC, 18:00 UTC, 06:00 UTC, and 06:00 UTC on 15 October, respectively. Precipitation from the P3 scheme was the closest to the 6 h cumulative precipitation. Figure 7b shows the hourly streamflow from the InfoWorks ICM in the simulation area; the response time to the precipitation input was approximately 6 h. The live flow had two peaks at 0800 UTC and 2000 UTC on 15 October, with a maximum value reaching 15.35 $m^3 \cdot s^{-1}$. The SBU_YLin and NSSL schemes generally captured both peaks, although the second peak was simulated in advance and the values were underestimated. The WDM6 and Lin schemes simulated the peaks, although the simulated flows between the two peaks were significantly overestimated. The WDM6 scheme underestimated the first peak flow, and the second peak was simulated in advance. The Lin scheme accurately captured the two peak flows, although the peak flow time was slightly delayed. The Thompson, Morrison, and WSM6 solutions captured both peaks but were delayed, underestimating the first peak and overestimating the second peak. The Milbrandt–Yau and P3 schemes performed well for peak flow and process flow, and the flood peak time was slightly delayed. The Milbrandt–Yau and P3 schemes slightly overestimated and underestimated the observations, respectively. Therefore, considering the peak time and flow processes, streamflow simulations of the Morrison and P3 schemes are generally preferable. The good performance of Morrison may be attributed to the realistic simulations of raindrops benefiting from the predictions of intercept parameters [38]. It is worth noting that P3 performs relatively the best in terms of flow simulations. The better performance of P3 may be attributed to the realistic time series of precipitation simulations, and this may be further attributed to the realistic prediction of ice particles as a result of the predictions of bulk rime mass fraction and density of rimed ice mass [39]. To quantitatively analyze the differences between the simulations of nine different cloud microphysical schemes in the InfoWorks ICM model and further compare the impact of cloud microphysical schemes on pipe network flow simulations, the hourly flow of the pipeline throughout 36 h was evaluated using statistical methods.

Except for the correlation coefficients of the SBU_YLin and Morrison schemes, which were lower than 0.42, the results of the schemes reached 0.5 and above. Among these, the P3 scheme reached 0.73, followed by Thompson, WDM6, and WSM6. The average deviation value indicates that all scheme simulations overestimated the streamflow observations, which was mainly due to the overestimated precipitation input to the model. Simultaneously, P3 also showed the minimum RMSE and maximum NSE at 2.6 and 0.48, respectively, indicating the high credibility of its simulations. Simulations of schemes other than WSM6 were generally credible; however, the error in the process simulation was large. The REP simulated by the WDM6 scheme was 2%, and the simulation was the best, followed by the

SBU_YLin, Lin, and NSSL schemes. The error for the P3 scheme was 26%. Thompson and WSM6 showed a minimum absolute error of 1.0, followed by the P3 and Lin schemes. From Figure 7b, this can be attributed to the overestimation of the second peak flow, which finally misjudged the flood peak. Both the P3 and WDM6 schemes fit the observed temporal patterns. Considering all the statistics together, the WDM6 scheme reproduced the flood peaks well but poorly simulated process flows, whereas the Lin and NSSL schemes were better at simulating process flows. The P3 scheme exhibits better performance than most of the other schemes applied in the study, excelling in both precipitation and hydrological simulations in the Haining county of Jiaxing in this study. The reasons for the best performance of P3 may be as follows. First, the advantages of the P3 microphysics scheme may account for it. Specifically, the P3 scheme avoids using artificial processes (e.g., auto-conversion), and it also uses a continuum of particle properties, limiting potential errors due to artificial thresholds [39]. This potentially results in the satisfactory simulations of total rainfall amounts and spatial variations in precipitation. In general, the P3 scheme is the best because it captures both flood peaks and flow processes well.
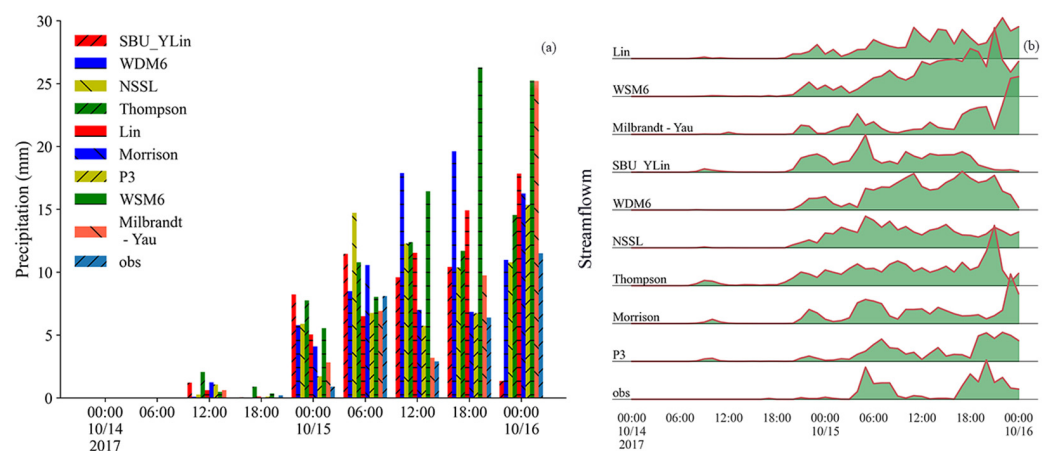

Figure 7. Time series of precipitation and streamflow simulated by different microphysical schemes in Haining district: (**a**) simulated incremental 6 h precipitation; (**b**) regional streamflow from the InfoWorks model, unit is m^3/s.

5. Conclusions and Discussions

This study used the WRF model to simulate the precipitation process of PREs related to Typhoon Khanun (2017) based on different cloud microphysical parameterization schemes. The InfoWorks ICM model was used to simulate the urban flooding process in Haining City during heavy rainfall, and the following precipitation results were evaluated as coupling variables:

(1) Based on the precipitation evaluations of the above examples, the 36 h rainfall distribution simulated by the NSSL and Lin schemes exhibited better results than those of other cloud microphysical parameterization schemes. The TS score results confirmed the above conclusion and indicated that the NSSL scheme is optimal. However, when applied the simulated precipitation from NSSL to the InfoWorks ICM model to simulate flooding, the results were not optimal.

(2) The InfoWorks ICM was used to establish an urban stormwater model for the study area. The results show that the P3 scheme is the best for simulating the flood peak and process flow, indicating that the model is more sensitive to rainfall process changes due to input precipitation and that the precipitation process of the WRF simulation results requires further comparison and evaluation.

(3) The atmospheric-hydrological model adopts a one-way coupling method with precipitation as the coupling variable. The results show that the optimal solution P3 exhibits an RMSE, correlation coefficient, and NSE of 2.6, 0.73, and 0.48, respectively.

Compared with the combined configuration of various physical parameters in WRF, the primary focus of this study was to analyze the impact of cloud microphysical schemes on broader atmospheric-hydrological processes. The current study found that several schemes, such as NSSL, which had higher precipitation simulation results, output precipitation for use in hydrological models to simulate flooding, and the results were not ideal. This is because the evaluation of precipitation results using the TS score mainly considers the intensity and spatial distributions of precipitation, ignoring the precipitation process that has a greater impact on urban flooding. The precipitation output of the P3 scheme with an average precipitation score performance is the best for the flooding simulation. This shows that, in future precipitation simulations, the intensity, landing area of precipitation, and time at which heavy precipitation occurs need to be comprehensively considered. Coupling meteorological models with urban flooding models must be considered to improve the accuracy of urban flooding simulations. The results indicate that merely selecting a precipitation scheme based on rainfall score is insufficient for rainfall applications in the hydrological models. When utilizing WRF simulation results for flood simulations, it is imperative to conduct a comprehensive evaluation of the simulated precipitation using various schemes as inputs in hydrological models, along with their corresponding simulated flows. This involves assessing the total precipitation amount, the timing of peak precipitation, and the spatial trends in precipitation.

In general, owing to the limitations of the calculation conditions and observational data, a case simulation of the PRE of Typhoon Khanun was conducted. As the conditions improve in the future, more cases can be selected for examination to obtain more valuable research results.

References

1. Cong, C.; Chen, L.; Lei, X.; Li, Y. A Study on the Mechanism of the Tropical Cyclone Remote Precipitation. *Acta Meteorol. Sin.* **2012**, *70*, 717–727.
2. Shanghai Typhoon Institute of China Meteorological Administration. *Climatological Atlas of Tropical Cyclones over the Western North Pacific (1981–2010)*; Science Press: Beijing, China, 2017.
3. Meng, Z.; Xu, X.; Chen, L. Mesoscale Characteristics of the Interaction between Tc Tim(9406) and Mid-Latitude Circulation. *Acta Meteorol. Sin.* **2002**, *60*, 31–39.
4. Cong, C.; Chen, L.; Lei, X.; Li, Y. An Overview on the Study of Tropical Cyclone Remote Rainfall. *J. Trop. Meteorol.* **2011**, *27*, 264–270.
5. Xu, H.; Li, X.; Yin, J.; Zhang, D. Predecessor rain events in the yangtze river delta region associated with south China sea and northwest pacific ocean (SCS-WNPO) tropical cyclones. *Adv. Atmos. Sci.* **2023**, *40*, 1021–1042. [CrossRef]
6. Son, Y.; Lorenzo, E.D.; Luo, J. WRF-hydro-CUFA: A scalable and adaptable coastal-urban flood model based on the WRF-hydro and SWMM models. *Environ. Model. Softw.* **2023**, *167*, 105770. [CrossRef]

7. Xia, Q.; Fan, Y.; Zhang, H.; Jiang, C.; Wang, Y.; Hua, X.; Liu, D. A Review on the Development of Two-Way Coupled Atmospheric-Hydrological Models. *Sustainability* **2023**, *15*, 2803. [CrossRef]

8. Wagner, S.; Fersch, B.; Yuan, F.; Yu, Z.; Kunstmann, H. Fully coupled atmospheric-hydrological modeling at regional and long-term scales: Development, application, and analysis of WRF-HMS. *Water Resour. Res.* **2016**, *52*, 3187–3211. [CrossRef]

9. Liu, Y.; Liu, J.; Li, C.; Yu, F.; Wang, W.; Qiu, Q. Parameter Sensitivity Analysis of the WRF-Hydro Modeling System for Streamflow Simulation: A Case Study in Semi-Humid and Semi-Arid Catchments of Northern China. *Asia-Pac. J. Atmos. Sci.* **2021**, *57*, 451–466. [CrossRef]

10. Song, H.-J.; Lim, K.-S.S. Evaluation of bulk microphysics parameterizations for simulating the vertical structure of heavy rainfall between Korea and the United States. *Weather. Clim. Extrem.* **2022**, *37*, 100490. [CrossRef]

11. Bauer, P.; Thorpe, A.; Brunet, G. The quiet revolution of numerical weather prediction. *Nature* **2015**, *525*, 47–55. [CrossRef]

12. Lord, S.J.; Willoughby, H.E.; Piotrowicz, J.M. Role of a Parameterized Ice-Phase Microphysics in an Axisymmetric, Nonhydrostatic Tropical Cyclone Model. *J. Atmos. Sci.* **1984**, *41*, 2836–2848. [CrossRef]

13. Xu, W.; Chen, H.; Wei, H.; Luo, Y.; Zhao, T. Extreme Precipitation Produced by Relatively Weak Convective Systems in the Tropics and Subtropics. *Geophys. Res. Lett.* **2022**, *49*, e2022GL098048. [CrossRef]

14. Gu, X.; Li, G. Impact of cloud microphysical schemes on numerical simulation of a plateau shear line rainstorm event. *J. Yunnan Univ. (Nat. Sci. Ed.)* **2019**, *41*, 526–536.

15. Pang, Q.; Ping, F.; Shen, X.; Liu, L. A Comparative Study of Effects of Different Microphysics Schemes on Precipitation Simulation for Typhoon Mujigae (2015). *Chin. J. Atmos. Sci.* **2019**, *43*, 202–220. [CrossRef]

16. Zhou, W.; Lu, C.; Gao, W.; Deng, L. A Modeling Study of the Evolution and Microphysical Mechanisms of a Warm-Sector Heavy Rainfall in South China. *J. Trop. Meteorol.* **2020**, *36*, 805–820. [CrossRef]

17. Liu, J.; Bray, M.; Han, D. A study on WRF radar data assimilation for hydrological rainfall prediction. *Hydrol. Earth Syst. Sci.* **2013**, *17*, 3095–3110. [CrossRef]

18. Wang, W.; Liu, J.; Xu, B.; Li, C.; Liu, Y.; Yu, F. A WRF/WRF-Hydro coupling system with an improved structure for rainfall-runoff simulation with mixed runoff generation mechanism. *J. Hydrol.* **2022**, *612*, 128049. [CrossRef]

19. Ravazzani, G.; Amengual, A.; Ceppi, A.; Homar, V.; Romero, R.; Lombardi, G.; Mancini, M. Potentialities of ensemble strategies for flood forecasting over the Milano urban area. *J. Hydrol.* **2016**, *539*, 237–253. [CrossRef]

20. Thorndahl, S.; Nielsen, J.E.; Jensen, D.G. Urban pluvial flood prediction: A case study evaluating radar rainfall nowcasts and numerical weather prediction models as model inputs. *Water Sci. Technol.* **2016**, *74*, 2599–2610. [CrossRef]

21. Xu, H.; Zhang, D.; Li, X. The Impacts of Microphysics and Terminal Velocities of Graupel/Hail on the Rainfall of Typhoon Fitow (2013) as Seen from the WRF Model Simulations with Several Microphysics Schemes. *J. Geophys. Res. Atmos.* **2021**, *126*, e2020JD033940. [CrossRef]

22. Xu, H.; Li, X. Torrential rainfall processes associated with a landfall of Typhoon Fitow (2013): A three-dimensional WRF modeling study. *J. Geophys. Res. Atmos.* **2017**, *122*, 6004–6024. [CrossRef]

23. Xu, H.; Zhang, D. Impacts of cloud radiative processes on the convective and stratiform rainfall associated with typhoon fitow (2013). *Front. Earth Sci.* **2022**, *16*, 1052–1060. [CrossRef]

24. Zhou, J.; Zhang, H.; Zhang, J.; Zeng, X.; Ye, L.; Liu, Y.; Tayyab, M.; Chen, Y. WRF model for precipitation simulation and its application in real-time flood forecasting in the Jinshajiang River Basin, China. *Meteorol. Atmos. Phys.* **2018**, *130*, 635–647. [CrossRef]

25. Hunt, K.M.R.; Menon, A. The 2018 Kerala floods: A climate change perspective. *Clim. Dyn.* **2020**, *54*, 2433–2446. [CrossRef]

26. Gu, Y.; Peng, D.; Deng, C.; Zhao, K.; Pang, B.; Zuo, D. Atmospheric–hydrological modeling for Beijing's sub-center based on WRF and SWMM. *Urban Clim.* **2022**, *41*, 101066. [CrossRef]

27. Liu, T.; Yu, J.; Meng, Q.; Wang, Y.; Zhang, X. Near-inertial oscillation response of typhoon 'Kanu' in the northeastern continental shelf of the South China Sea. *Mar. Forecast.* **2022**, *39*, 83–89.

28. Jin, Q.; Li, W. Influence Analysis of Typhoon Khanun to Ningbo City. *China Water Resour.* **2018**, *841*, 35–36.

29. Duan, J.; Qian, Y.; Jiang, J.; Wang, Y.; Wu, Z. Causes of Rainstorm Enhancement in Northeastern Zhejiang Related with Typhoon Khanun Landing in Guangdong Province. *J. Arid Meteorol.* **2020**, *38*, 737–746.

30. Chen, S.-H.; Sun, W.-Y. A One-dimensional Time Dependent Cloud Model. *J. Meteorol. Soc. Jpn. Ser. II* **2002**, *80*, 99–118. [CrossRef]

31. Hong, S.-Y.; Lim, J.-O.J. The WRF Single-Moment 6-Class Microphysics Scheme (WSM6). *Asia-Pac. J. Atmos. Sci.* **2006**, *42*, 129–151.

32. Milbrandt, J.A.; Yau, M.K. A Multimoment Bulk Microphysics Parameterization. Part I: Analysis of the Role of the Spectral Shape Parameter. *J. Atmos. Sci.* **2005**, *62*, 3051–3064. [CrossRef]

33. Milbrandt, J.A.; Yau, M.K. A Multimoment Bulk Microphysics Parameterization. Part II: A Proposed Three-Moment Closure and Scheme Description. *J. Atmos. Sci.* **2005**, *62*, 3065–3081. [CrossRef]

34. Lin, Y.; Colle, B.A. A New Bulk Microphysical Scheme That Includes Riming Intensity and Temperature-Dependent Ice Characteristics. *Mon. Weather Rev.* **2011**, *139*, 1013–1035. [CrossRef]

35. Lim, K.-S.S.; Hong, S.-Y. Development of an Effective Double-Moment Cloud Microphysics Scheme with Prognostic Cloud Condensation Nuclei (CCN) for Weather and Climate Models. *Mon. Weather Rev.* **2010**, *138*, 1587–1612. [CrossRef]

36. Mansell, E.R.; Ziegler, C.L.; Bruning, E.C. Simulated Electrification of a Small Thunderstorm with Two-Moment Bulk Microphysics. *J. Atmos. Sci.* **2010**, *67*, 171–194. [CrossRef]

37. Thompson, G.; Field, P.R.; Rasmussen, R.M.; Hall, W.D. Explicit Forecasts of Winter Precipitation Using an Improved Bulk Microphysics Scheme. Part II: Implementation of a New Snow Parameterization. *Mon. Weather Rev.* **2008**, *136*, 5095–5115. [CrossRef]

38. Morrison, H.; Thompson, G.; Tatarskii, V. Impact of Cloud Microphysics on the Development of Trailing Stratiform Precipitation in a Simulated Squall Line: Comparison of One- and Two-Moment Schemes. *Mon. Weather Rev.* **2009**, *137*, 991–1007. [CrossRef]

39. Morrison, H.; Milbrandt, J.A. Parameterization of Cloud Microphysics Based on the Prediction of Bulk Ice Particle Properties. Part I: Scheme Description and Idealized Tests. *J. Atmos. Sci.* **2015**, *72*, 287–311. [CrossRef]

40. Khain, A.; Lynn, B.; Dudhia, J. Aerosol Effects on Intensity of Landfalling Hurricanes as Seen from Simulations with the WRF Model with Spectral Bin Microphysics. *J. Atmos. Sci.* **2010**, *67*, 365–384. [CrossRef]

41. Lou, Y.; Wang, P.; Li, Y.; Wang, L.; Chen, C.; Li, J.; Hu, T. Management of the designed risk level of urban drainage system in the future: Evidence from haining city, China. *J. Environ. Manag.* **2024**, *351*, 119846. [CrossRef]

42. Pan, J.; Chen, Y.; Tang, W.; Wang, L.; Wang, P.; Hu, T. InfoWorks icm-based simulative study on rainstorm waterlogging for Asian Games venues in Lin'An District. *Water Resour. Hydropower Eng.* **2023**, *54*, 12–21. [CrossRef]

43. Su, Z.; Li, L.; Ren, F.; Zhu, J.; Liu, C.; Wan, Q.; Sun, Q.; Jia, L. Study of Landfalling Typhoon Potential Maximum Gale Forecasting in South China. *Atmosphere* **2023**, *14*, 888. [CrossRef]

44. Tan, M.L.; Santo, H. Comparison of GPM IMERG, TMPA 3B42 and PERSIANN-CDR satellite precipitation products over Malaysia. *Atmos. Res.* **2018**, *202*, 63–76. [CrossRef]

45. Yuan, J.; Zhao, D.; Yang, R.; Yang, H. Predecessor rain events over China's low-latitude highlands associated with Bay of Bengal tropical cyclones. *Clim. Dyn.* **2018**, *50*, 825–843. [CrossRef]

46. Xu, H.; Li, X.; Yin, J.; Zhou, L.; Song, Y.; Hu, T. Microphysics affect the sensitivities of rainfall to different horizontal-resolution simulations: Evidence from a case study of the Weather Research and Forecasting model runs. *Atmos. Res.* **2023**, *296*, 107022. [CrossRef]

47. Liu, T.; Chen, Y.; Chen, S.; Li, W.; Zhang, A. Mechanisms of the transport height of water vapor by tropical cyclones on heavy rainfall. *Weather Clim. Extrem.* **2023**, *41*, 100587. [CrossRef]